# Anomalous-dispersion phase matching in a hypergap crystal

Kun Chen , 1,2 Xiaolei Hu, 1,2 Zhengran Wu, 1,2 Xiang Guo, 1,2 Zhilin Li, 1,\* and Ling Lu 1, 1 Institute of Physics, Chinese Academy of Sciences/Beijing National Laboratory for Condensed Matter Physics, Beijing 100190, China School of Physical Sciences, University of Chinese Academy of Sciences, Beijing 100049, China

(Received 8 April 2025; accepted 20 August 2025; published 9 October 2025)

While two perfect phase-matching mechanisms exist in homogeneous single crystals, birefringent phase-matching (BPM) dominates for nonlinear optical applications. The anomalous-dispersion phase matching (ADPM), though demonstrated in gases and liquids, has not been established in crystals due to the parasitic material absorption that induces the anomalous dispersion in the first place. This absorption bottleneck can be overcome by a crystal possessing an additional spectral gap in its absorption spectrum, beyond the regular band gap, which we term the "hypergap". Here, we theoretically propose and experimentally demonstrate such a hypergap and the ADPM-enabled third harmonic generation in potassium chromate  $K_2CrO_4$ . Our results introduce a class of nonlinear optical materials that do not rely on lattice anisotropy or periodic poling.

DOI: 10.1103/hnf1-vj2r

## I. INTRODUCTION

Phase matching, a crucial condition dictated by photon momentum conservation, is essential for efficient nonlinear parametric processes such as harmonic generations, wave mixings, parametric amplifiers, parametric oscillators, and parametric down-conversions [1–3]. Most applications take place in transparent crystals satisfying either the birefringence phase matching (BPM) or the quasi-phase-matching. The quasi-phase-matching utilizes micropatterns and structural momentum to compensate for the momentum mismatch between photons [4–8]. This process requires precision microfabrication and is theoretically less ideal than the BPM, often referred to as the perfect phase matching [9]. Perfect phase matching, in the case of the second and third harmonic generations, requires equal refractive indices at different frequencies,  $n(\omega) = n(2\omega)$  or  $n(3\omega)$ . Due to the normal dispersion in transparent crystals, perfect phase matching is typically achieved only through crystalline birefringence, where the refractive indices for orthogonal polarizations can match at different wavelengths as shown in Fig. 1(a).

There exists a second kind of perfect phase matching, known as the anomalous-dispersion phase matching (ADPM), as illustrated in Fig. 1(b). Anomalous dispersion, taking place within an absorption peak where the index decreases with frequency, can be used to cancel the normal material dispersion and match the indices across the absorption peak. ADPM was previously studied by dissolving the dye molecules in solutions [10,11], by dispersing alkali vapors in a noble gas [12], by mixing chromophores inside a polymer thinfilm waveguide [13], and by doping lanthanide ions into the host-insulator powders [14]. In these studies, the dopants are chosen to have a strong and narrow absorption peak between

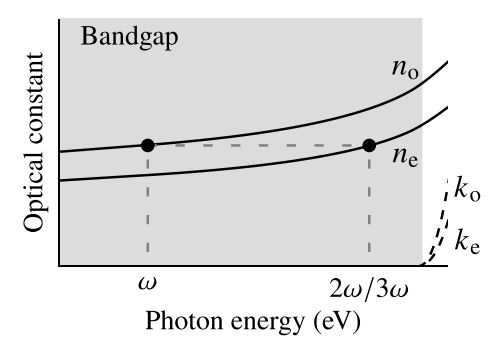
\*Contact author: lizhilin@iphy.ac.cn †Contact author: linglu@iphy.ac.cn

the fundamental and harmonic wavelengths. Unfortunately, such doping approaches suffer from nonuniform distribution and residual absorptions. Ideally, if ADPM could be realized in an intrinsic crystal without absorption, it would potentially be a highly efficient way for nonlinear generation. Compared to BPM, ADPM eliminates the interaction-length limitation imposed by beam walk-off, allows access to larger principal elements of the nonlinear tensor for the same polarizations, and removes the requirements on material birefringence and the precise cutting angles of the crystals. In this work, we demonstrate ADPM in a stoichiometric single crystal featuring a hypergap [15]: a low-loss spectral window beyond the conventional band gap, shown in Fig. 1(b). The anomalous dispersion takes place in the absorption region separating the band gap and hypergap, so that the refractive indices in the two gaps can match. In the rest of the paper, we combine theoretical prediction, material synthesis, and comprehensive optical characterizations to show that potassium chromate (K<sub>2</sub>CrO<sub>4</sub>) is a hypergap insulator capable of supporting ADPM, enabling third-harmonic generation (THG) of unique spectral and polarization properties.

## II. THEORETICAL PREDICTION

We identify that the inversion-symmetric  $\beta$ -phase  $K_2CrO_4$  [16] is a hypergap crystal. As shown in Fig. 2(a), each unit cell consists of four  $CrO_4^{2-}$  tetrahedron. In the band structure in Fig. 2(b), the multiple narrow bands close to the Fermi level originate from the  $Cr\ d$ -orbitals and the  $O\ p$ -orbitals. The band gap  $(E_g)$  is the energy from the top of the valence band to the bottom of the conduction band. The definition of hypergap involves two more energy bands, below the valence band and above the conduction band, that we refer to as the hypervalence and hyperconduction bands. The transition energy from valence-band bottom to the top of the conduction band is W, which is the lower band edge of the hypergap. The upper band edge of the hypergap is defined by the smaller

## (a) Birefringence phase matching (BPM)



## (b) Anomalous-dispersion phase matching (ADPM)

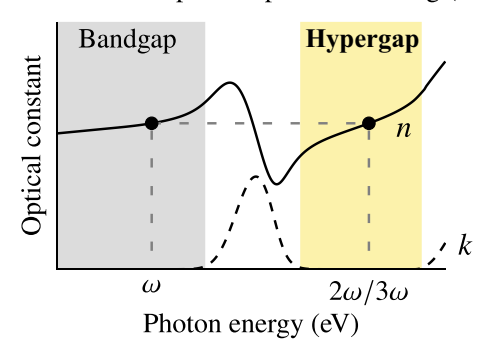


FIG. 1. Two perfect phase-matching schemes. (a) BPM, the refractive index of the fundamental wave equals that of the harmonic wave for different polarization states, both in the band gap. (b) ADPM, the refractive index of the fundamental wave in the band gap equals that of the harmonic wave in the hypergap for the same polarization state. The solid and dashed lines represent the real (n) and imaginary (k) parts of the refractive index.

transition energy between  $G_v$  (the transition from the hypervalence-band top to conduction-band bottom) and  $G_c$  (the transition from the valence-band top to hyper-conduction-band bottom). When  $G = \min\{G_v, G_c\} > W$ , the hypergap opens, which is evident from the zero joint density of states (JDOS) in Fig. 2(c). Consequently, the optical transition is forbidden in both the band gap and hypergap.

 $K_2CrO_4$  fulfills the ADPM condition for THG, as shown in Fig. 2(c) where the refractive index in the band gap equals that in the hypergap. This is possible since the absorption between the two gaps is strong enough to produce sufficient anomalous dispersion. Since the crystal has inversion [space group No. 62 (*Pnma*)], second-harmonic generation is disallowed. Although the  $K_2CrO_4$  is orthorhombic, the anisotropy is low as the difference in  $\varepsilon_{xx}$ ,  $\varepsilon_{yy}$ , and  $\varepsilon_{zz}$  is around 5% in Fig. 2(c). The above *ab initio* calculations are performed using the Vienna *Ab initio* Simulation Package (VASP) [17] with the generalized gradient approximation [18].

## III. CRYSTAL GROWTH

The potassium chromate is used in the industry of enameling, electroplating, and anticorrosion treatments [19]. We purchased K<sub>2</sub>CrO<sub>4</sub> from Aladdin Reagent Co. Ltd. with a purity above 99% and an average grain size of 0.2 mm. These powders are dissolved in deionized water at 90° C.

The crystals precipitate from the saturated solution by slow cooling. After a day, cuboid crystals of millimeter sizes are obtained, as shown in Fig. 3(a). The observed transparency and the characteristic yellow color suggest that the crystal does not absorb around the yellow wavelength ( $\sim$ 2.2 eV), indicating a band gap slightly above this value. Single-crystal x-ray diffraction is performed on the sample, and a complete summary of details is provided in Appendix A.

### IV. ELLIPSOMETRY AND TRANSMISSION

The optical constants are measured by spectroscopic ellipsometry and plotted in Fig. 3(b). The extinction coefficient (k) shows the presence of the hypergap (3.95 to 4.05 eV) in addition to the band gap (2.6 eV), in which the k values are vanishingly small. Moreover, the refractive index (n) in the hypergap aligns with that in the band gap and their frequencies differ by a factor of 3, indicating the satisfaction of the ADPM condition for THG. The ellipsometry data are well fitted with 12 Gaussian oscillators assuming material isotropy [20] and an effective-medium model to account for surface roughness. Though the phase velocity (n) matches between the two gaps, the group velocity  $(n_g)$  is higher in the hypergap as shown in Fig. 3(c). Interestingly, the group velocity dispersion (GVD) turns negative in the hypergap [15], which is not available in band-gap materials at optical wavelengths. This intrinsic anomalous GVD could open new venues for generating solitons and manipulating ultrafast pulses [21].

We take transmission measurements on the K<sub>2</sub>CrO<sub>4</sub> samples to verify the frequencies and transparencies of their hypergap and band gap. The high transmittance ( $\sim$ 70%) through a thick sample ( $\sim$ 1 mm) below 2.6 eV is observed in Fig. 3(d), indicating the band-gap absorption edge around the corresponding blue wavelength (~480 nm). The less transparent hypergap is revealed by the 10% transmittance at 4 eV through a thin sample of  $\sim 10 \, \mu m$  thick, consistent with the ellipsometry results in Fig. 3(e). The broadband reflectance is also measured to be low (~10%) across the relevant wavelength range. Although the hypergap is not as transparent as the band gap, the absorption length ( $\sim 10 \,\mu m$ ) is still long enough for us to observe the THG in K2CrO4. Because the harmonic signal in the hypergap can be generated in the last few microns without absorption before exiting the sample, as the pump light in the band gap propagates through the whole sample.

## V. THIRD-HARMONIC GENERATION

After knowing the phase-matching wavelengths from ellipsometry and their propagation lengths from transmission, we perform the THG experiment by pumping in the band gap and detecting in the hypergap with the setup shown in Appendix B. We tune the output wavelength of the femtosecond laser near the phase-matching wavelength of  $\sim 930$  nm, whose spectral full width at half maximum (FWHM) is 20 nm. The third-harmonic signal is detected at  $\sim 310$  nm (FWHM of 4 nm), close to the least absorptive wavelength in the hypergap, as shown in Fig. 3(e). The signal light can be observed as a weak blue spot when shining on a white paper. The cubic intensity dependence between the pump and signal, in Fig. 3(f),

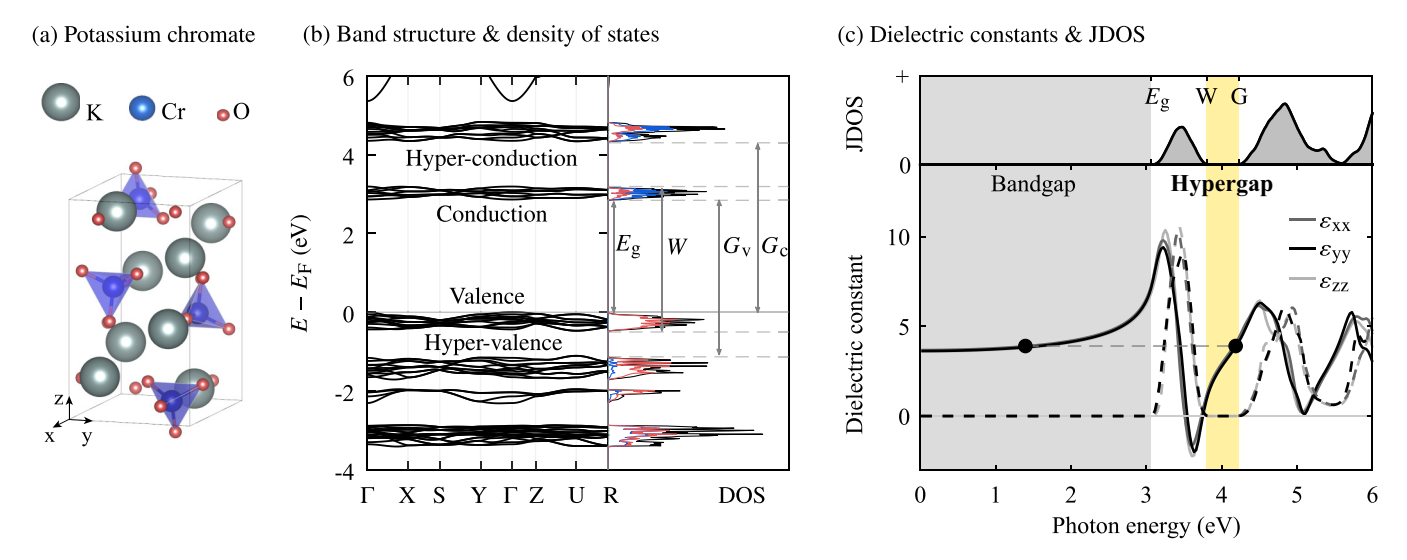


FIG. 2. Prediction of hypergap and ADPM in  $K_2CrO_4$ . (a) Crystal structure. (b) Band structure and DOS of potassium chromate show multiple isolated narrow bands. (c) Both the joint density of states (JDOS, convolution of DOS) and dielectric constants show the presence of a hypergap beyond the band gap, in which phase matching is satisfied for THG.

confirms that the generated signal arises from a third-order nonlinear process.

To verify whether the THG process is due to phase matching, we observe how the THG spectra respond to the tuning of the pump wavelength across the phase-matching point from 900 nm to 945 nm. Shown in Fig. 4(a), when the pump wavelength deviates from 930 nm, the harmonic amplitude drops

quickly. This is expected for a phase-matched process when the wavelength is detuned from the optimal matching point. To compare ADPM with the traditional BPM, we design a control experiment using the centrosymmetric  $\alpha$ -barium borate (BBO) supporting THG at identical wavelengths. As shown in Fig. 5(a) of Appendix C, the BPM-enabled THG amplitude exhibits a slower decay rate relative to  $K_2CrO_4$  under

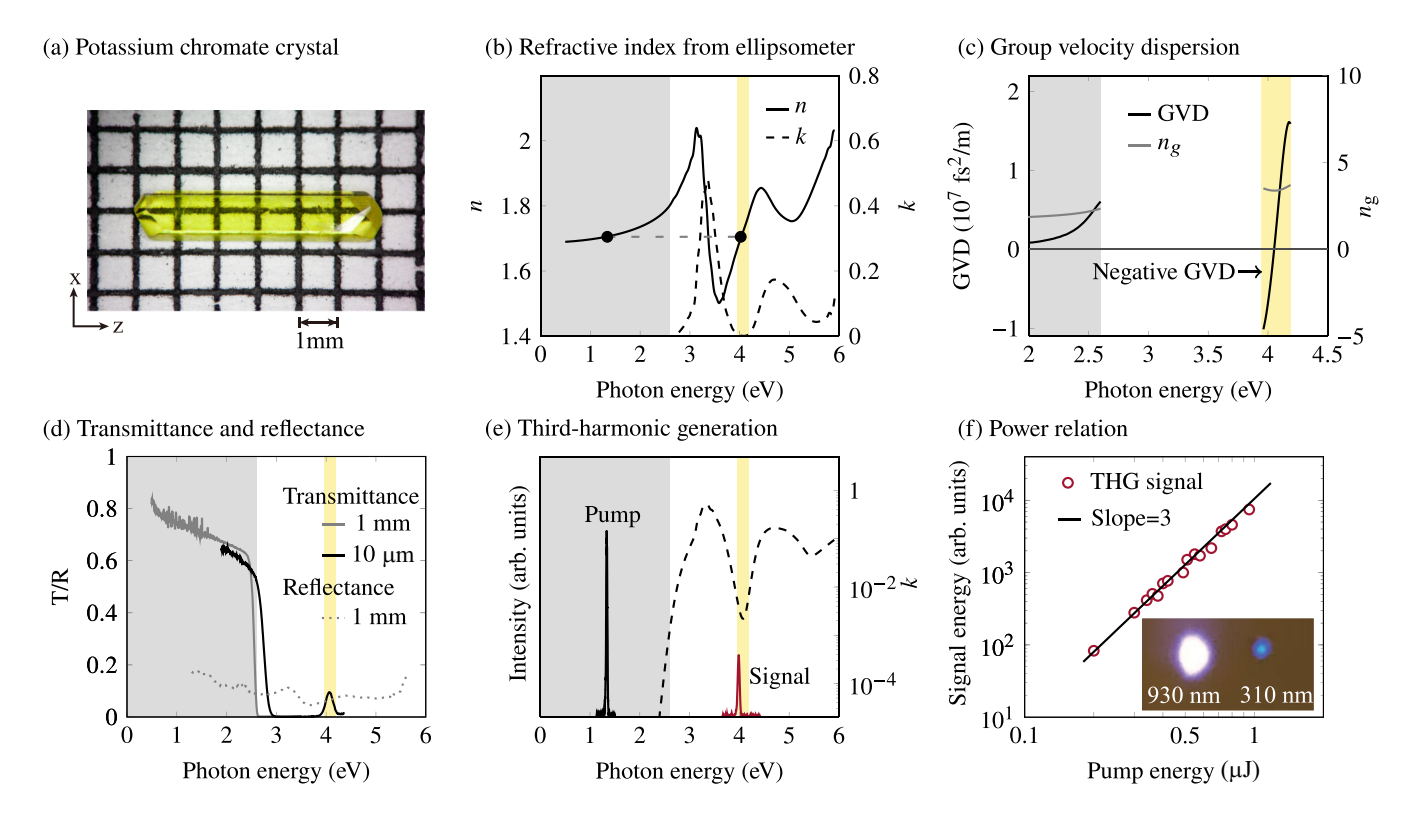


FIG. 3. Observing ADPM-enabled THG in the hypergap of  $K_2CrO_4$ . (a) Crystal sample. (b) Refractive index from ellipsometry exhibiting the hypergap and ADPM. (c) GVD and group index  $(n_g)$  in the band gap and hypergap. (d) The transmittance and reflectance of samples with different thicknesses. (e) Spectral wavelengths of the pump and THG signal. (f) Power relation between the THG signal and pump. The inset shows the beam patterns of both pump and signal on a white paper. Logarithmic scale is used for the y axes of (e) (right) and (f).

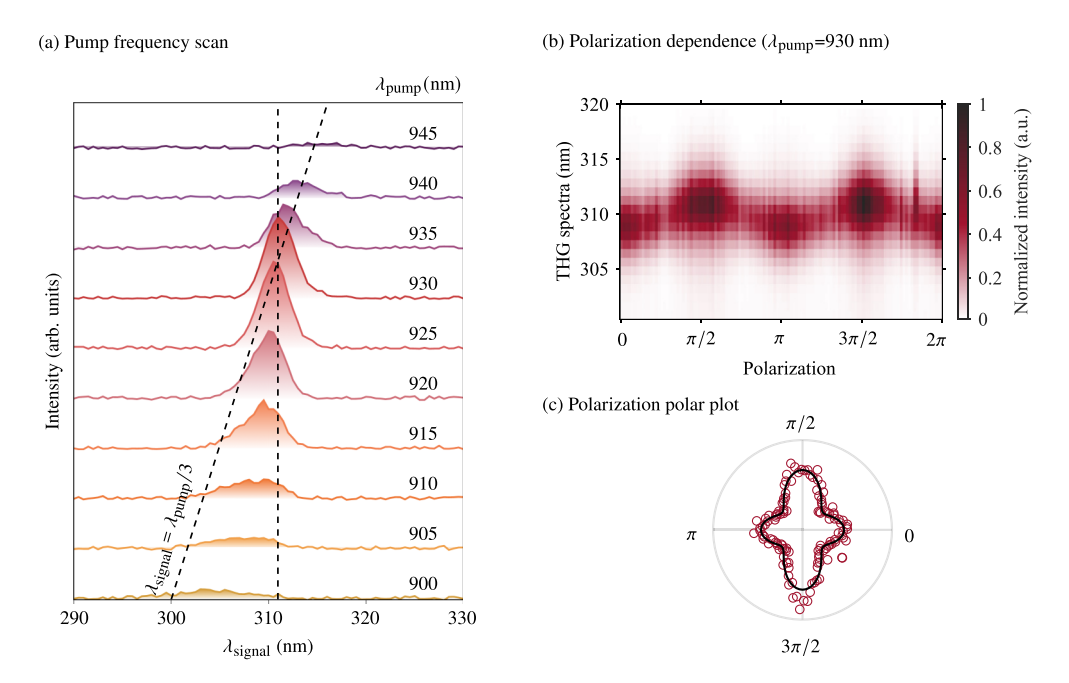


FIG. 4. Spectral and polarization characteristics of ADPM in  $K_2CrO_4$ . (a) THG spectra as a function of pump wavelength. (b) THG spectra as a function of pump polarization. (c) Polarization-resolved polar plot of the THG intensity spectrally integrated from (b).

pump frequency detuning. The difference between Figs. 4(a) and 5(a) reveals that the ADPM has a greater wavelength sensitivity compared to the BPM since the refractive index is more dispersive in the hypergap as opposed to the band gap shown in Figs. 1, 2(c), and 3(b). When we elevate the sample temperature from 300 K to 500 K, the ADPM wavelength redshifts 4 nm, estimated from the change of refractive index detailed in Appendix D.

## VI. POLARIZATION DEPENDENCE

A key difference between ADPM and BPM lies in their polarization dependence because the ADPM can be achieved between the same polarization states while BPM cannot. As expected for BPM, the THG intensity from  $\alpha$ -BBO vanishes at a certain polarization angle of the pump as shown in Fig. 5(b) and 5(c) of Appendix C. In stark contrast, ADPM could be completely insensitive to pump polarization, if the hypergap

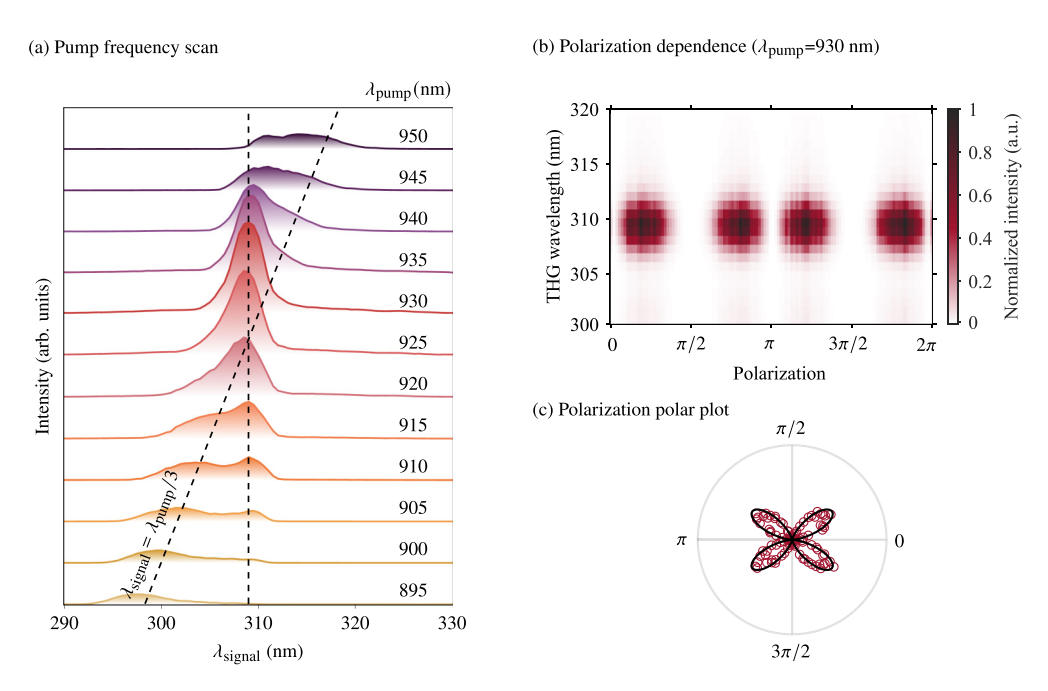


FIG. 5. Wavelength and polarization characteristics of BPM in  $\alpha$ -BBO. (a) THG spectra as a function of pump wavelength. (b) THG spectra as a function of pump polarization. (c) Polarization-resolved polar plot of the THG intensity spectrally integrated from (b).

crystal is cubic or isotropic without birefringence, as shown in Appendix E.

In Fig. 4(b), we plot the spectra of the THG signal, when the pump polarization is rotated using a half-wave plate. The central wavelength of the harmonic signal oscillates between 311 nm and 308 nm, reflecting the slight birefringence in the orthorhombic K<sub>2</sub>CrO<sub>4</sub> crystal predicted in Fig. 2(c). In Fig. 4(c), we integrate the spectral intensity of THG from Fig. 4(b) into a polar plot as a function of pump polarization. The resulting nodeless pattern of ADPM is in direct contrast to the nodal pattern of BPM in Appendix C Fig. 5(c). The experimental nodeless pattern in Figs. 4(b) and 4(c) can be modeled and reproduced by considering all types of phasematchings in K<sub>2</sub>CrO<sub>4</sub>, as we derive in Appendix F.

### VII. CONCLUSION

We introduce the ADPM as a phase-matching mechanism in solids, facilitated by the hypergap, the second transparent window beyond the conventional band gap. This work paves the way for exploring parametric processes of ADPM and inspires the discovery of hypergap crystals with unique optical properties [15,22].

### ACKNOWLEDGMENTS

We thank Dongxiang Zhang and Qiulin Zhang for their help. This work was supported by the Natural Science Foundation of China (Grant No. 12025409), by the Chinese Academy of Sciences through the Project for Young Scientists in Basic Research (Grant No. YSBR-021), through the Youth Innovation Promotion Association (Grant No. 2021008), and through the IOP-HKUST-Joint Laboratory for Wave Functional Materials Research.

## DATA AVAILABILITY

The data that support the findings of this article are not publicly available. The data are available from the authors upon reasonable request.

# APPENDIX A: X-RAY DIFFRACTION

Single-crystal x-ray diffraction is performed on a  $K_2CrO_4$  specimen ( $\lambda=0.71073$  Å) at 273(2) K. A total of 6444 reflections are collected, of which 648 are independent ( $R_{int}=6.56\%$ , completeness = 99.5%). The structure is solved by direct methods and refined by full-matrix least squares on  $F^2$  within the orthorhombic space group Pnma (Z=4). Final refinement yield  $R_1=2.04\%$  [ $I>2\sigma(I)$ ],  $wR_2=5.80\%$ , and a goodness-of-fit of 1.237. The refined lattice parameters are a=7.6644(5) Å, b=5.9230(5) Å, c=10.3909(8) Å, with a calculated density of 2.735 g/cm<sup>3</sup>. Absorption correction is applied using the multiscan method (SADABS). The residual electron density ranged from -0.398 to 0.468 e/Å<sup>3</sup>.

Tables I–IV summarize the crystal parameters, data collection settings, and refinement statistics for the  $K_2CrO_4$  structure reported in this work.

TABLE I. Data collection details for K<sub>2</sub>CrO<sub>4</sub>.

Parameter	Omega scan	Phi scan	
dx (mm)	50.102	50.102	
$2\theta$ (deg)	24.41	24.37	
$\omega$ (deg)	-67.26	284.11	
$\phi$ (deg)	-52.36	98.27	
χ (deg)	3.09	22.00	
Width (deg)	0.50	0.50	
Frames	368	328	
Time (s)	10	10	
Voltage	50 kV	50 kV	
Current 1.1 mA		1.1 mA	

## APPENDIX B: OPTICAL SETUP

As shown in Fig. 6, a 930-nm pulse is produced by a femtosecond Ti:sapphire laser system (centered at 800 nm, 1 kHz, 120 fs) equipped with a TOPAS Prime optical parametric amplifier. A filter blocks the residual 800-nm pump. A half-wave plate and a Glan-Taylor prism are used to control either the beam energy in THG or the polarization of the incident light in polarization-dependent THG, depending on the experimental configuration. Lenses focus the beam for THG, and a UV filter (FGUV11-UV) filters the pump signal.

#### APPENDIX C: BBO CONTROL EXPERIMENT

To compare ADPM with BPM, we repeat the ADPM experiments in Fig. 4 using  $\alpha$ -BBO (centrosymmetric) and plot the BPM results in Fig. 5. We design the THG wavelength of  $\alpha$ -BBO to be roughly the same as that of  $K_2CrO_4$ . We adopted the type-II ( $\rho=54.1^\circ, \phi=30^\circ$ ) phase matching because type I has a low nonlinear susceptibility (thus efficiency) and type III cannot be achieved around 310 nm in  $\alpha$ -BBO [23]. Here  $\rho$  is the phase-matching angle and  $\phi$  is the azimuth angle. The  $\alpha$ -BBO crystal of dimensions 0.5 mm  $\times$  3 mm is fabricated and mounted by CASTECH INC.

The pump frequency scan of the THG in  $\alpha$ -BBO is shown in Fig. 5(a). Like in  $K_2CrO_4$ , the designed phase-matching peak at 309 nm diminishes as the pump wavelength shifts away from 930 nm. Unlike in  $K_2CrO_4$ , a satellite peak shifting

TABLE II. Crystal data for K<sub>2</sub>CrO<sub>4</sub>.

Formula weight	194.20 g/mol	
Temperature	273(2) K	
Wavelength	0.71073 Å	
Crystal system	Orthorhombic	
Space group	Pnma	
Unit cell dimensions	a = 7.6644(5) Å,	$lpha=90^\circ$
	b = 5.9230(5) Å,	$eta=90^\circ$
	c = 10.3909(8)  Å,	$\gamma=90^\circ$
Unit cell volume	$471.71(6) \text{ Å}^3$	
Z	4	
Density (calculated)	$2.735 \text{ g/cm}^3$	
Absorption coefficient	$4.079~{\rm mm^{-1}}$	
F(000)	376	

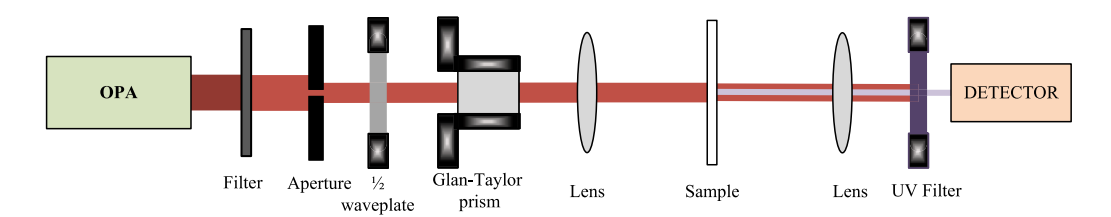


FIG. 6. Schematic setup for demonstrating ADPMed THG.

with the pump wavelength is always visible. This difference indicates that the ADPM is more precise to wavelength than BPM due to the stronger material dispersion in the hypergap than that in the band gap.

The polarization dependence of the THG experiment for  $\alpha$ -BBO is shown in Figs. 5(b) and 5(c). We rotate the pump polarization angle ( $\theta$ ) when its central wavelength is fixed at 930 nm. The polarization dependence and the nodal pattern of the type-II (ooe-e) phase-matching process follow  $\cos^4(\theta) \sin^2(\theta)$ , as we derive in Appendix F.

# APPENDIX D: TEMPERATURE DEPENDENCE OF REFRACTIVE INDEX

Shown in Fig. 7, temperature-dependent ellipsometry measurements are performed on potassium chromate in the range of 300 K to 500 K. With increasing temperature, the crystal color gradually changes from yellow to orange due to the redshift of the band gap. A concurrent redshift of approximately 4 nm was also observed in the THG phasematching wavelength.

TABLE III. Structure refinement details for K<sub>2</sub>CrO<sub>4</sub>.

$\theta$ range for data collection	3.30° to 28.50°
Index ranges	$-9 \leqslant h \leqslant 10$ ,
	$-7 \leqslant k \leqslant 7$ ,
	$-13 \leqslant l \leqslant 13$
Reflections collected	6444
Independent reflections	$648 (R_{\rm int} = 0.0656)$
Coverage of independent reflections	99.5%
Absorption correction	Multiscan (SADABS)
Structure solution method	Direct methods
Solution program	SHELXT 2014/5
Refinement method	Full-matrix least squares on $F^2$
Refinement program	SHELXL-2018/3
Data / restraints / parameters	648 / 0 / 41
Goodness-of-fit on $F^2$	1.237
Final <i>R</i> indices $[I > 2\sigma(I)]$	$R_1 = 0.0204, wR_2 = 0.0571$
Final R indices (all data)	$R_1 = 0.0248, wR_2 = 0.0580$
Weighting scheme	$w = 1/[\sigma^2(F_a^2) + (0.0286P)^2$
	+0.0697P]
	where $P = (F_o^2 + 2F_c^2)/3$
Extinction coefficient	0.1030(60)
Largest diff. peak / hole	+0.398/-0.468 (e/Å <sup>3</sup> )
RMS deviation from mean	$0.105  (e/Å^3)$

## APPENDIX E: POLARIZATION PATTERNS OF THG

ADPM is the only way to phase-match (type 0) in an isotropic medium without birefringence, which is independent of the polarization of the pump laser. If birefringence is introduced, other types of phase matching in BPM also occur with nodal polarization patterns summarized in Fig. 8.

#### APPENDIX F: POLARIZATION DEPENDENCE OF ADPM

Here, we derive the polarization-dependent patterns observed in the THG experiments due to ADPM in potassium chromate.

A linearly polarized wave of the angle  $\theta$  to the x principal axis propagating along the z-principal axis in an orthorhombic crystal can be expressed as two orthogonal fundamental waves: an x-polarized wave with refractive index  $n_x$  and a y-polarized wave with refractive index  $n_y$ ,

$$\mathbf{E}_{x}(\omega, z) = E_{x}(\omega, z)\hat{\mathbf{a}}_{x}(\omega)e^{ik_{x}z} = E_{0}(\omega, z)\cos\theta\hat{\mathbf{a}}_{x}(\omega)e^{ik_{x}z},$$

$$\mathbf{E}_{y}(\omega, z) = E_{y}(\omega, z)\hat{\mathbf{a}}_{y}(\omega)e^{ik_{y}z} = E_{0}(\omega, z)\sin\theta\hat{\mathbf{a}}_{x}(\omega)e^{ik_{x}z}.$$
(F1)

The symbols x and y denote the polarizations of the fundamental waves along the principal axes x and y, with wave vectors  $k_x = n_x \omega/c$  and  $k_y = n_y \omega/c$ , respectively. Here,  $\hat{\mathbf{a}}$  represents the unit polarization vector of each mode. The third-order polarization in a crystal is given by

$$\mathbf{P}^{(3)}(3\omega, z)$$

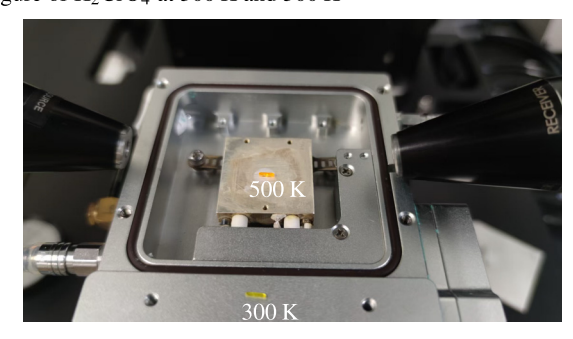
$$= \varepsilon_0 \sum_{j,k,l \in \{x,y\}} \mathbf{\chi}^{(3)}(3\omega, \omega, \omega, \omega) \mathbf{E}_j(\omega, z) \mathbf{E}_k(\omega, z) \mathbf{E}_l(\omega, z)$$
(F2)

Here  $\mathbf{E}_{j}(\omega, z)$ ,  $\mathbf{E}_{k}(\omega, z)$ ,  $\mathbf{E}_{l}(\omega, z)$  can each represent either of the fundamental polarization states  $\mathbf{E}_{x}(\omega, z)$  or  $\mathbf{E}_{y}(\omega, z)$ . Under the slowly varying amplitude approximation, the

TABLE IV. Atomic coordinates and equivalent isotropic atomic displacement parameters (Å<sup>2</sup>) for K<sub>2</sub>CrO<sub>4</sub>.  $U_{eq}$  is defined as one third of the trace of the orthogonalized  $U_{ij}$  tensor.

Atom	x/a	y/b	z/c	$U_{ m eq}$
Cr01	0.27089(5)	0.75	0.42052(3)	0.01270(16)
K002	0.98905(6)	0.25	0.19995(6)	0.01979(18)
K003	0.83462(7)	0.75	0.41450(6)	0.02465(19)
O004	0.1979(3)	0.75	0.56943(17)	0.0285(4)
O005	0.1982(2)	0.5231(2)	0.34708(13)	0.0309(3)
O006	0.4838(3)	0.75	0.4197(2)	0.0327(5)

## (a) Figure of K<sub>2</sub>CrO<sub>4</sub> at 300 K and 500 K



#### (b) Temperature-dependent refractive index

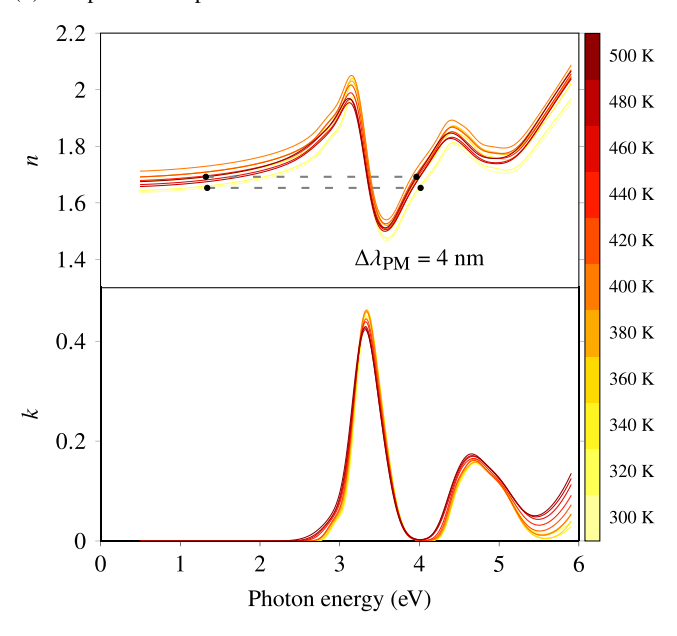


FIG. 7. (a) Picture of the  $K_2CrO_4$  orange crystal at the center of the chuck at 500 K, between the two focusing elements of the ellipsometer. The yellow crystal at the edge of the stage is at room temperature. (b) Temperature-dependent refractive index (n and k) spectra of  $K_2CrO_4$  from 300 K to 500 K. A redshift of 4 nm is observed in the phase-matching wavelength for THG across this temperature range.

wave-coupling equation of third-harmonic generation can be expressed as

$$\frac{\partial E_u(3\omega, z)}{\partial z} = \frac{i\mu_0(3\omega)^2}{2k_{3x}} \hat{\mathbf{a}}_u(3\omega) \vdots \mathbf{P}^{(3)}(3\omega, z) e^{-ik_u z}.$$
 (F3)

Here,  $\varepsilon_0$  and  $\mu_0$  represent the vacuum permittivity and vacuum permeability, respectively. The symbol  $u \in \{x, y\}$  denotes

the polarization direction of the third-harmonic electric field. Substituting Eq. (F2) into Eq. (F3), we have

$$\frac{\partial E_u(3\omega, z)}{\partial z} = \frac{i3\omega}{2n_u c} \sum_{j,k,l \in \{x,y\}} \chi_{ujkl}^{(3)} E_j(\omega) E_k(\omega) E_l(\omega) e^{i\Delta k_{ujkl} z},$$
(F4)

where

$$\Delta k_{ujkl}(\omega) = k_i(\omega) + k_j(\omega) + k_l(\omega) - k_u(3\omega),$$
 (F5) and

$$\chi_{uikl}^{(3)} = \hat{\mathbf{a}}_u(3\omega) \cdot \chi^{(3)}(3\omega, \omega, \omega, \omega) \vdots \hat{\mathbf{a}}_j(\omega) \hat{\mathbf{a}}_k(\omega) \hat{\mathbf{a}}_l(\omega).$$
 (F6)

The different  $\chi^{(3)}$  coefficients represent different combinations of the fundamental and output polarized fields. Note that in an orthorhombic crystal,  $\chi^{(3)}_{xxxy} = \chi^{(3)}_{xyyy} = \chi^{(3)}_{yxxx} = \chi^{(3)}_{yxyy} = 0$  (see Eq. (1.5.72) in Ref. [3]). This implies the absence of type-I and type-III phase-matched THG processes. Assuming the *z*-independent pump amplitude, we have

$$E_x(\omega, z) = E_x(\omega),$$

$$E_y(\omega, z) = E_y(\omega),$$

$$E_u(3\omega, 0) = 0.$$
(F7)

Substituting the fundamental wave solution from Eq. (F1) into the coupled-wave equation Eq. (F4) and performing the integration over the interaction length z, we obtain the third-harmonic electric field components for both x and y polarizations.

$$E_{x}(3\omega, z) = \frac{i3\omega z}{2n_{3x}c} \Big[ \cos^{3}\theta \chi_{xxxx}^{(3)} e^{i\Delta k_{xxxx}z/2} \operatorname{sinc}(\Delta k_{xxxx}z/2) \\ + 3\cos\theta \sin^{2}\theta \chi_{xxyy}^{(3)} e^{i\Delta k_{xxyy}z/2} \operatorname{sinc}(\Delta k_{xxyy}z/2) \Big] \\ \times E_{0}(\omega)^{3},$$

$$E_{y}(3\omega, z) = \frac{i3\omega z}{2n_{3y}c} \Big[ 3\cos^{2}\theta \sin\theta \chi_{yyxx}^{(3)} e^{i\Delta k_{yyxx}z/2} \operatorname{sinc}(\Delta k_{yyxx}z/2) \\ + \sin^{3}\theta \chi_{yyyy}^{(3)} e^{i\Delta k_{yyyy}z/2} \operatorname{sinc}(\Delta k_{yyyy}z/2) \Big] E_{0}(\omega)^{3}.$$
(F8)

Here  $\operatorname{sinc}(x) = \sin(x)/x$ . In Eq. (F8), the electric fields of THG in x and y polarizations are generated by processes of type 0 and type II. Then the total intensity of THG in Eq. (F9) comprises contributions from type 0 (xxx-x, yyy-y), type II (xxy-y, yyx-x) and their cross terms

$$I(3\omega, z) = I_{x}(3\omega, z) + I_{y}(3\omega, z) = \frac{9\omega^{2}}{\varepsilon_{0}^{2}c^{4}n_{1}^{3}}I_{0}^{3}(\omega, 0)z^{2}\frac{1}{n_{3x}}\left[\cos^{6}\theta\left(\chi_{xxxx}^{(3)}\right)^{2}\operatorname{sinc}^{2}(\Delta k_{xxxx}z/2)\right]$$

$$+ 6\cos^{4}\theta\sin^{2}\theta\chi_{xxxx}^{(3)}\chi_{xxyy}^{(3)}\operatorname{sinc}(\Delta k_{xxxx}z/2)\operatorname{sinc}(\Delta k_{xxyy}z/2) + 9\cos^{2}\theta\sin^{4}\theta\left(\chi_{xxyy}^{(3)}\right)^{2}\operatorname{sinc}^{2}(\Delta k_{xxyy}z/2)\right]$$

$$+ \frac{1}{n_{3y}}\left[9\cos^{4}\theta\sin^{2}\theta\left(\chi_{yyxx}^{(3)}\right)^{2}\operatorname{sinc}^{2}(\Delta k_{yyxx}z/2) + 6\cos^{2}\theta\sin^{4}\theta\chi_{yyxx}^{(3)}\chi_{yyyy}^{(3)}\operatorname{sinc}(\Delta k_{yyxx}z/2)\operatorname{sinc}(\Delta k_{yyyy}z/2)\right]$$

$$+ \sin^{6}\theta\left(\chi_{yyyy}^{(3)}\right)^{2}\operatorname{sinc}^{2}(\Delta k_{yyyy}z/2)\right].$$
(F9)

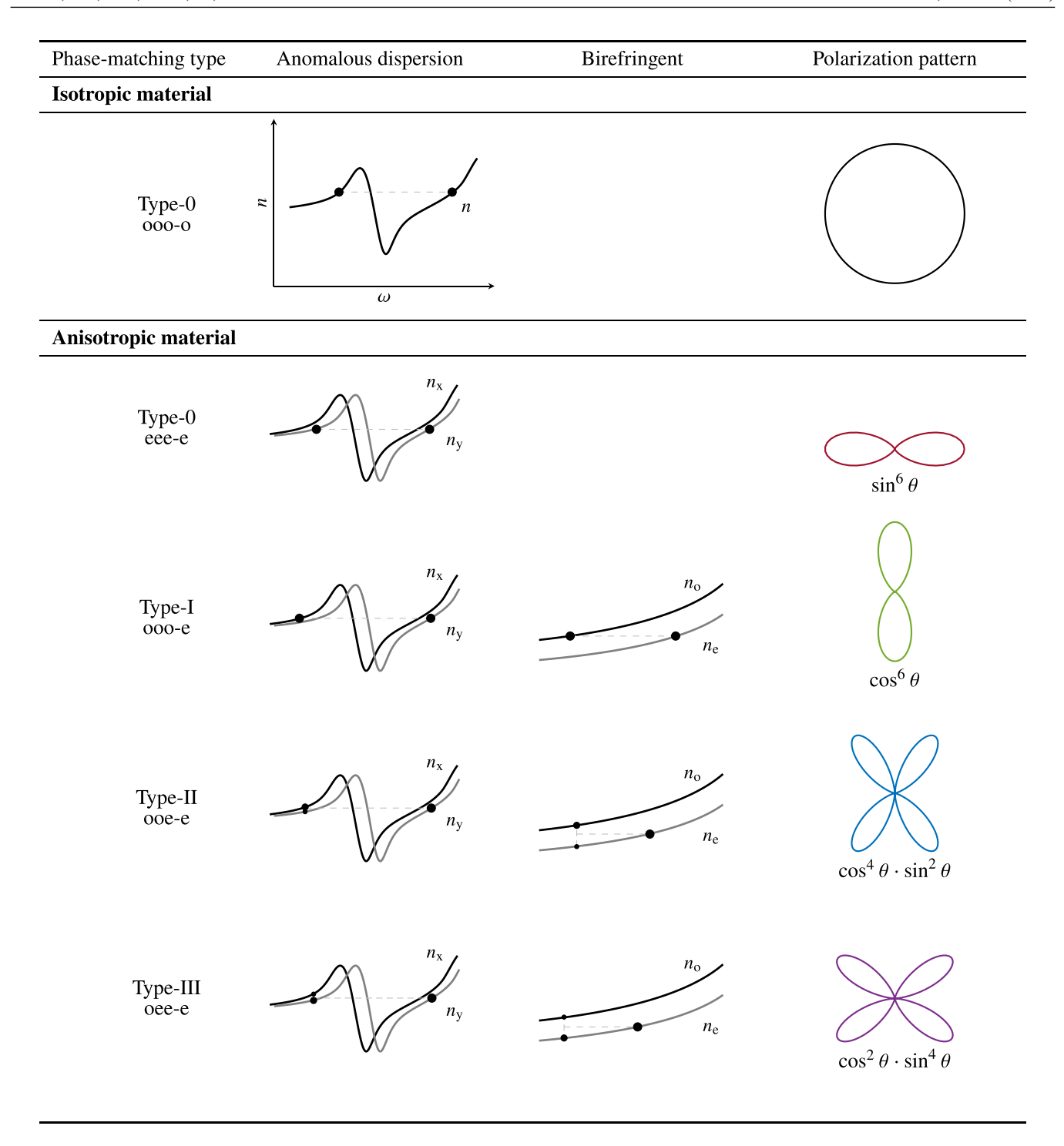


FIG. 8. All types of ADPM and BPM in isotropic and anisotropic materials and their THG patterns under pump polarization rotation.

In an isotropic material,  $\chi_{xxxx} = \chi_{yyyy} = 3\chi_{xxyy} = 3\chi_{yyxx}$  (see Eq. (1.5.38) in Ref. [3]), and the distinction between x and y directions vanishes, i.e.,  $\Delta k_{xxxx} = \Delta k_{xxyy} = \Delta k_{yyxx} = \Delta k_{yyyy}$  and  $n_{3x} = n_{3y}$ . In this case, Eq. (F9) becomes

$$I(3\omega, z) = \frac{9\omega^2}{\varepsilon_0^2 c^4 n_1^3 n_3} I_0^3(\omega, 0) z^2 (\chi_{xxxx}^{(3)})^2 \operatorname{sinc}^2(\Delta k_{xxxx} z/2).$$
(F10)

Equation (F10) demonstrates polarization independence and the circular polar pattern shown in Figs. 8 and 9, expected for isotropic systems.

In anisotropic materials, different types of nonlinear optical processes in Eq. (F9) phase match at different wavelengths, as in Fig. 8. In  $K_2CrO_4$  with low anisotropy, these wavelengths fall within the vicinity of the pump laser spectrum, allowing several different harmonic generation processes

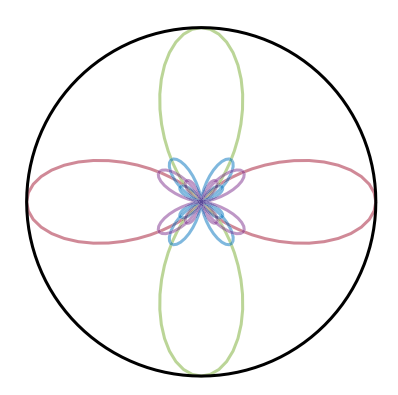


FIG. 9. The circular pattern of THG, versus rotation of pump polarization, recovered in the limit of isotropic material.

to occur simultaneously and form noncircular polarization patterns.

We substitute the following experimental conditions into Eq. (F9): a detected Gaussian spectral fundamental intensity with a 20-nm bandwidth, a center wavelength of 930 nm, and a sample length of 10  $\mu$ m. The wave-vector mismatch  $\Delta k$  is determined by tuning the refractive indices  $n_x$  and  $n_y$  using ellipsometry data of potassium chromate. We also assume  $\chi_{xxxx} = \chi_{yyyy} = 7\chi_{xxyy} = 7\chi_{yyxx}$ .

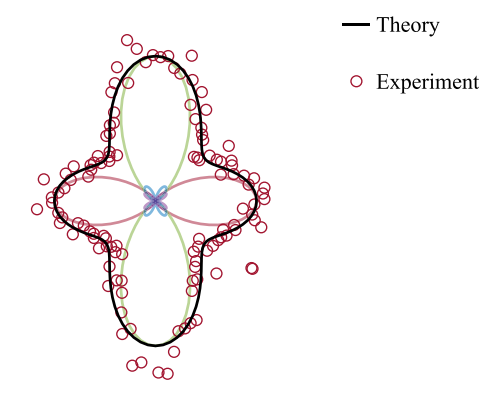


FIG. 10. Polarization-dependent THG pattern for  $K_2CrO_4$ . The six contributing terms in Eq. (F9) reproduce the experimental angular dependence of the pump polarization.

In Fig. 10, we reproduce the experimental THG polarization pattern in  $K_2CrO_4$ . The polarization pattern of THG is dominated by type-0 phase matching (xxx-x, yyy-y) along its two principal axes, with additional contributions from the type-II phase matching and the cross terms between type 0 and type II.

- [1] N. Bloembergen, *Nonlinear Optics* (World Scientific, Singapore, 1996).
- [2] Y. R. Shen, *Principles of Nonlinear Optics* (Wiley-Interscience, New York, 1984).
- [3] R. Boyd, *Nonlinear Optics* (Elsevier Science, Amsterdam, 2020).
- [4] L. E. Myers, R. Eckardt, M. Fejer, R. Byer, W. Bosenberg, and J. Pierce, Quasi-phase-matched optical parametric oscillators in bulk periodically poled LiNbO<sub>3</sub>, J. Opt. Soc. Am. B **12**, 2102 (1995).
- [5] S. N. Zhu, Y. Y. Zhu, and N. B. Ming, Quasi-phase-matched third-harmonic generation in a quasi-periodic optical superlattice, Science 278, 843 (1997).
- [6] M. Baudrier-Raybaut, R. Haidar, P. Kupecek, P. Lemasson, and E. Rosencher, Random quasi-phase-matching in bulk polycrystalline isotropic nonlinear materials, Nature (London) 432, 374 (2004).
- [7] X. Zhao, H. Long, H. Xu, J. Kougo, R. Xia, J. Li, M. Huang, and S. Aya, Nontrivial phase matching in helielectric polarization helices: Universal phase matching theory, validation, and electric switching, Proc. Natl. Acad. Sci. USA 119, e2205636119 (2022).
- [8] H. Hong, C. Huang, C. Ma, J. Qi, X. Shi, C. Liu, S. Wu, Z. Sun, E. Wang, and K. Liu, Twist phase matching in two-dimensional materials, Phys. Rev. Lett. 131, 233801 (2023).
- [9] J. Armstrong, N. Bloembergen, J. Ducuing, and P. S. Pershan, Interactions between light waves in a nonlinear dielectric, Phys. Rev. 127, 1918 (1962).
- [10] P. P. Bey, J. F. Giuliani, and H. Rabin, Generation of a phasematched optical third harmonic by introduction of anomalous

- dispersion into a liquid medium, Phys. Rev. Lett. **19**, 819 (1967).
- [11] P. A. Cahill, K. D. Singer, and L. A. King, Anomalousdispersion phase-matched second-harmonic generation, Opt. Lett. 14, 1137 (1989).
- [12] J. F. Young, G. Bjorklund, A. Kung, R. Miles, and S. Harris, Third-harmonic generation in phase-matched Rb vapor, Phys. Rev. Lett. 27, 1551 (1971).
- [13] T. C. Kowalczyk, K. D. Singer, and P. A. Cahill, Anomalousdispersion phase-matched second-harmonic generation in a polymer waveguid, Opt. Lett. 20, 2273 (1995).
- [14] M. T. Anderson, M. L. Phillips, and G. D. Stucky, Inorganic materials for anomalous-dispersion phase-matched second-harmonic generation: Rubidium titanyl arsenate isomorphs, Rb[Ti<sub>1-2x</sub>Ln<sub>x</sub>Nb<sub>x</sub>]OAsO<sub>4</sub>, J. Non-Cryst. Solids **178**, 120 (1994).
- [15] X. Hu, X. Guo, Z. Wu, K. Chen, X. Chen, Z. Li, and L. Lu, Hypergap optical materials, Adv. Mater. e12769 (2025).
- [16] J. A. McGinnety, Redetermination of the structures of potassium sulphate and potassium chromate: The effect of electrostatic crystal forces upon observed bond lengths, Acta Crystallogr. B: Struct Crystallogr Cryst. Chem. 28, 2845 (1972).
- [17] G. Kresse and J. Furthmüller, Efficiency of *ab-initio* total energy calculations for metals and semiconductors using a plane-wave basis set, Comput. Mater. Sci. 6, 15 (1996).
- [18] J. P. Perdew, K. Burke, and M. Ernzerhof, Generalized gradient approximation made simple, Phys. Rev. Lett. 77, 3865 (1996).

- [19] H. J. Lunk, Discovery, properties and applications of chromium and its compounds, ChemTexts 1, 6 (2015).
- [20] D. E. Aspnes, Approximate solution of ellipsometric equations for optically biaxial crystals, J. Opt. Soc. Am. **70**, 1275 (1980).
- [21] A. Weiner, *Ultrafast Optics* (John Wiley & Sons, New York, 2011), Vol. 72.
- [22] Z. Wu, C. Li, X. Hu, K. Chen, X. Guo, Y. Li, and L. Lu, Hypergap transparent conductor, Nat. Mater. 24, 1387 (2025).
- [23] M. Shi, G. Zhang, B. Li, R. Li, T. Yan, M. Luo, and N. Ye, Efficient frequency conversion for cubic harmonic generation at 266 nm in centrosymmetric α-BBO crystal, Opt. Lett. **43**, 1734 (2018).